Electro-optically programmable photonic circuits enabled by wafer-scale integration on thin-film lithium niobate

Yong Zheng,[1,2] Haozong Zhong,[1,2] Haisu Zhang,[2] Lvbin Song,[1,2] Jian Liu,[1,2] Youting Liang,[1,2] Zhaoxiang Liu,[2] Jinming Chen,[2] Junxia Zhou,[1,2] Zhiwei Fang,[2] Min Wang,[2] Lin Li,[2] Rongbo Wu,[2,*] and Ya Cheng[1,2,3,4,5,6,7,†]

[1]*State Key Laboratory of Precision Spectroscopy, East China Normal University, Shanghai 200062, China*
[2]*The Extreme Optoelectromechanics Laboratory (XXL), School of Physics and Electronic Science, East China Normal University, Shanghai 200241, China*
[3]*State Key Laboratory of High Field Laser Physics and CAS Center for Excellence in Ultra-intense Laser Science, Shanghai Institute of Optics and Fine Mechanics (SIOM), Chinese Academy of Sciences (CAS), Shanghai 201800, China*
[4]*Collaborative Innovation Center of Extreme Optics, Shanxi University, Taiyuan 030006, China*
[5]*Collaborative Innovation Center of Light Manipulations and Applications, Shandong Normal University, Jinan 250358, China*
[6]*Shanghai Research Center for Quantum Sciences, Shanghai 201315, China*
[7]*Hefei National Laboratory, Hefei 230088, China*

(Received 1 May 2023; revised 17 July 2023; accepted 6 September 2023; published 22 September 2023; corrected 20 October 2023)

Programmable photonic circuits performing universal linear-optical transformations underpin vital functions in photonic quantum information processing, quantum-enhanced sensor networks, machine learning, and many other intriguing applications. Recent advances in photonic integrated circuits facilitate monolithic integration of externally controlled Mach-Zehnder interferometers (MZIs) which can implement arbitrary unitary transformation on a large number of input/output modes. In this work, we demonstrate a 4×4 programmable linear photonic circuit on lithium niobate on an insulator platform employing fast, power-efficient, and low-loss electro-optical phase shifters, showing enormous advantages in terms of configuration rate and power consumption. Our device composed of cascaded MZIs possesses a total on-chip power dissipation of only 1.5 mW when operating at 100 MHz modulation rate. Our MZIs exhibit high bandwidth of 22.5 GHz, fast switching with 160-ps rise time and 120-ps fall time, low insertion loss of 0.15 dB, and on-chip extinction ratio of −34 dB for both cross and bar routes.

DOI: 10.1103/PhysRevResearch.5.033206

I. INTRODUCTION

Benefiting from their compact footprint, high computation speed, low power consumption, sustainable scalability, and high phase stability, programmable linear photonic circuits composed of cascaded Mach-Zehnder interferometers (MZIs) to perform the general special unitary group of degree N [i.e., SU(N)] are becoming increasingly important in emerging applications such as photonic quantum information processing, quantum-enhanced sensors, optical neural network, and machine learning [1–8]. Stringent requirements are raised by these emerging applications on very large-scale photonic integration (VLSPI) and high-performance on-chip components, such as optical modulators with extremely low losses, ultrahigh switching speed, and high power efficiency. Owing to the maturing complementary-metal-oxide-semiconductor (CMOS) compatible very large-scale integration (VLSI) processes of high scalability and low manufacturing cost, material platforms including silicon-on-insulator (SOI), silicon nitride, and indium phosphide (InP) have been prevalently investigated with proof-of-concept demonstration [1–3,9–18]. Despite the great progresses made so far on such highly scalable material platforms, unprecedented challenges in maintaining a reasonable power consumption and propagation loss become more and more difficult to meet with the ever-increasing scale of programmable photonic circuits. The relatively high power consumption combined with the relatively slow tuning speed roots in the lack of intrinsic electro-optic effect in most semiconductor material platforms, making it necessary to use thermo-optic or piezo-optomechanical tuning for realizing the phase modulation in the fabricated photonic circuits [19].

Due to its excellent electro-optic and nonlinear optical properties, relatively high refractive index, and wide transparency window, lithium niobate ($LiNbO_3$, LN) has been pursued as an ideal material for photonic applications since the 1960s. Formidable challenges have existed for decades in obtaining high-quality LN thin films as well as forming high-quality photonic structures during the LN dry etching

*rbwu@phy.ecnu.edu.cn
†ya.cheng@siom.ac.cn

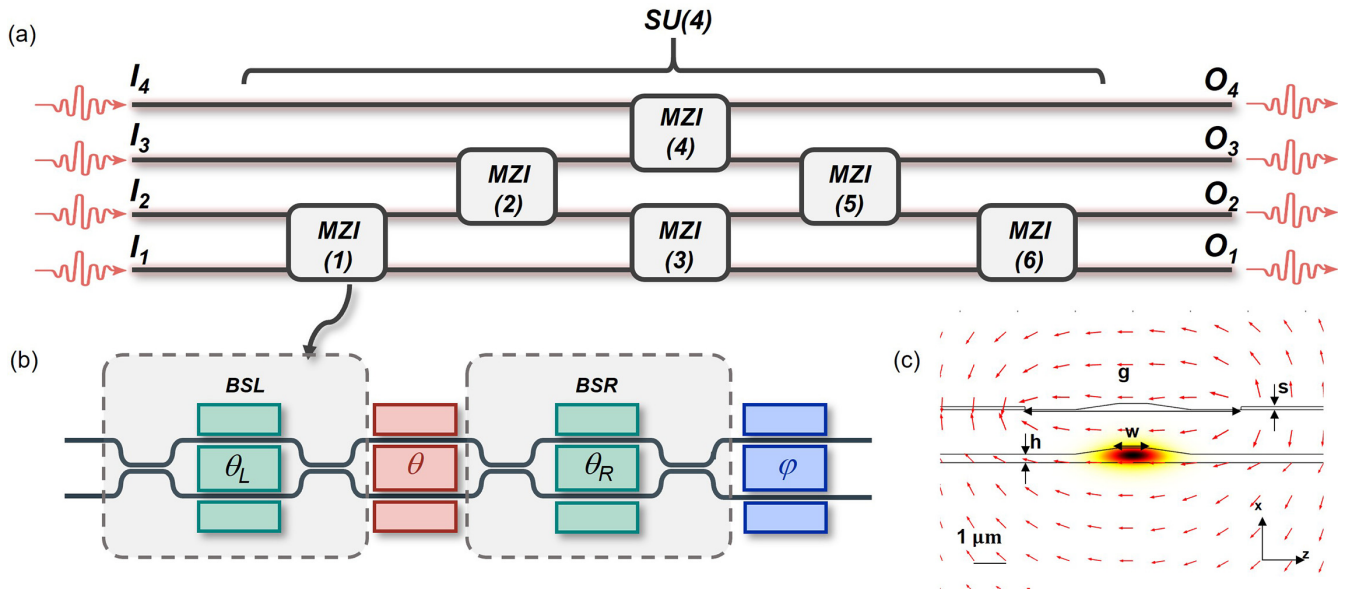

FIG. 1. (a) The arbitrary SU(4) composed of MZI units (1)–(6) that construct the 4 × 4 programmable linear photonic circuit. (b) Example MZI unit which functions as a perfect SU(2) using Miller's algorithm. (c) The simulated optical mode profile and electrical field shown by red arrows ($g = 7$ μm, $s = 210$ nm, $w = 1.0$ μm, $h = 290$ nm).

process with the quest for dense and high-performance photonic integration. With the advent of commercially available thin-film LN wafers prepared by ion slicing and the rapid advances in thin-film LN fabrication techniques, an abundance of optical components have been developed on the lithium niobate on isolator (LNOI) platform [20–26], including high-performance meter-scale long waveguides with propagation losses as low as 3 dB/m [27,28] and high-speed efficient electro-optical modulators with tens of gigahertz bandwidth and low power consumption below 1 fJ bit^{-1} [22]. The LNOI platform has also demonstrated efficiently periodically polarized lithium niobate (PPLN) wavelength converters [29], optical frequency combs [30], and active optical devices, such as lasers [31] and amplifiers [32], making it an ideal platform for integrated photonic circuits incorporating multiple functionalities. As compared to the established CMOS-compatible material platforms, LNOI fulfills all the stringent device requirements raised by programmable photonic circuits by its nature. Wafer-scale LNOI photonic integrated circuits conforming to the requirement on VLSPI have been fabricated with deep ultraviolet lithography (DUV) while maintaining low optical propagation loss of 27 dB/m [33]. Meanwhile, photolithography assisted chemomechanical etching (PLACE) technology [34], which patterns the hard mask with maskless femtosecond laser direct writing and then etches the LN with chemomechanical polishing (CMP), has also emerged as a promising technique for VLSPI LNOI devices production. PLACE is capable of manufacturing a wafer-scale device with high fabrication uniformity, competitive production rate, and very low optical propagation loss (i.e., ∼2.5 dB/m), enabled by the synergetic actions of high average power femtosecond laser and large-range motion stage together with the extremely smooth interface etched by the CMP process [28].

In this work, we demonstrate an MZI-based 4 × 4 programmable linear photonic circuit on the LNOI platform fabricated using the PLACE technology. Our MZI unit shows an electro-optical bandwidth of 22.5 GHz, and a fast switching speed of 160 ps rise time and 120 ps fall time. Our device achieves a low total on-chip power dissipation of only 1.5 mW when operating at a 100-MHz modulation rate, an insertion loss of 0.15 dB for each MZI unit, and full compensation of the imperfect parameters caused by fabrication fluctuations using Miller's calibration algorithm [31]. To the best of our knowledge, the demonstrated programmable photonic circuit has the largest integration scale of any reported LNOI-based devices so far, and outperforms its counterparts based on other material platforms in essential functional features such as response time, insertion loss, and power consumption, holding great promise in emerging classical and quantum applications.

II. DESIGN PRINCIPLE AND DEVICE REALIZATION

Figure 1(a) schematically illustrates the programmable linear photonic circuit composed of an array of MZI units (1)–(6). Using a two-dimensional subspace within a four-dimensional Hilbert space $[D_{\mathrm{MZI}}]_{4\times4}$ to define the unitary transformation matrix of the MZIs (1)–(6), a SU(4) can be constructed based on Reck *et al.*'s configuration [19]. The device illustrated in Fig. 1(a) constructs a transformation matrix $[D]_{4\times4}$ that linearly converts the input signal vector $[I]_{4\times1}$ to the output signal vector $[O]_{4\times1}$. Figure 1(b) exemplifies the experimental implementation of one MZI unit, featuring a tandem connection of two MZIs with an intermediate phase shifter (θ) and an output phase shifter (φ). The two MZIs (BSL and BSR) play the role of adjustable directional couplers controlled by internal phase shifters (θ_L and θ_R). Following Miller's algorithm, such tandem MZI design allows delicate tuning of the nonperfect splitting of directional couplers subject to fabrication errors to the perfect 50-50 splitting ratios, thereby a perfect SU(2) transformation is realized by each MZI unit despite the existence of a global transmission loss.

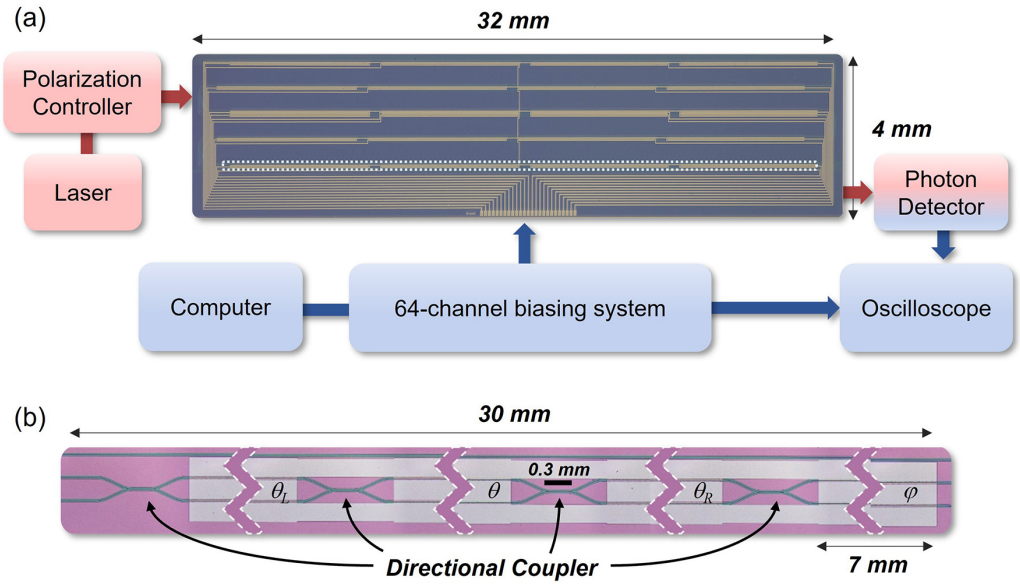

FIG. 2. (a) The arbitrary SU(4) transformation consisting of 24 phase modulators that can be tuned individually and six reconfigurable MZI units. (b) The microscope picture of an entire programmable MZI unit with extra phase shifters θ_L and θ_R.

Our device is fabricated on a X-cut 4-inch LNOI wafer with a 500-nm-thick LN layer bonded to a buried silica (SiO_2) layer on the 500-μm-thick silicon support (NANOLN) using PLACE technology. The details of the fabrication process can be found in our previous work [28,35]. The photograph of the fabricated programmable linear photonic circuit captured with a digital camera is shown in the center of Fig. 2(a). The arbitrary SU(4) transformation is realized by six reconfigurable MZI units including 24 phase modulators which can be addressed individually. In our device, all phase shifters utilize electro-optical (EO) actuation of LN with crystal Z axis lying in the horizontal plane and being oriented perpendicular to the waveguides. With such a configuration, the ground-signal-ground (GSG) electrodes will exert an electric field with equal strength but opposite direction in the two arms of each MZI when applying a voltage, resulting in a phase difference between light transmitted in the two arms. The simulated optical and electrical field profiles are shown in Fig. 1(c).

The internal structure of each MZI unit is further illustrated in Fig. 2(b), where each phase modulator is approximately 7 mm long and the total length of the MZI unit is ∼30 mm. It has been measured in our experiment that the optical loss of a single directional coupler is ∼0.02 dB, and the propagation loss of the optical waveguides with electrodes is ∼0.025 dB/cm [28], giving rise to the total optical loss of 0.15 dB for a reconfigurable MZI unit. The fiber-chip coupling loss of our device is about 7 dB/facet, which can be substantially reduced in the future by using spot size convertors (SSCs). For confining the SU(4) transformation circuits within the 4-in. wafer, the device is folded four times over a 32 mm × 4 mm chip area. The relatively large device footprint compared to SOI platforms is mainly due to the relatively low voltage efficiency of the purely linear EO modulator based on Pockels effects and the moderate LN-to-silica refractive index contrast. This is a trade-off for the overwhelming advantages of electro-optical effects in terms of configuration rate and power consumption. It should be pointed that there is no sacrifice in transmission loss despite our MZI is nearly two orders of magnitude longer compared to those on the best performing device based SOI [2], thanks to the low optical absorption of LN and the extremely smooth waveguide sidewalls produced by the PLACE technology. On the other hand, by taking the advantage of PLACE technology's unique ability on the meter-scale continuous lithography, ultralarge-scale chip processing with extremely low optical loss is now possible.

III. DEVICE CALIBRATION AND CHARACTERIZATION

The fabricated programmable photonic circuit normally features random phase offsets and nonperfect splitting ratios due to the inevitable fabrication process fluctuations. Thus, all the MZIs in the device must be calibrated before being programmed for a particular application. The calibration process is carried out based on the topology and order of the MZI units in the device with the experimental setup illustrated in Fig. 2(a). As shown in Fig. 3(a), the whole process for calibrating the internal phase shifters begins with MZI units (4)–(6) (red box), and then MZI units (2) and (3) (blue box) before MZI unit (1) (green box).

To characterize the reconfiguration speed of the fabricated device, we selected the path I_4-O_3 and the MZI unit (5) and measured the transmission versus voltage plot as shown in Fig. 3(d). The result shows a half-wave voltage (V_π) of 4.64 V, as well as extinction ratios of −36 dB and −34 dB for the bar route (I_4-O_3) and the cross route (I_4-O_2), respectively. When the MZI unit (4) was set in the cross state, a 100-MHz square-wave voltage with a peak-to-peak voltage of 4.4 V generated by an arbitrary waveform generator (AWG) and amplified by an electronic amplifier was exerted on the internal phase shifter of MZI unit (5). We performed the same test on a single MZI unit manufactured using the same technology. Figure 3(b) shows the measured curve of transmission versus time, indicating a rise time of 500 ps and a fall time of 1.7 ns for MZI unit (5) and a rise time of 160 ps and a fall time

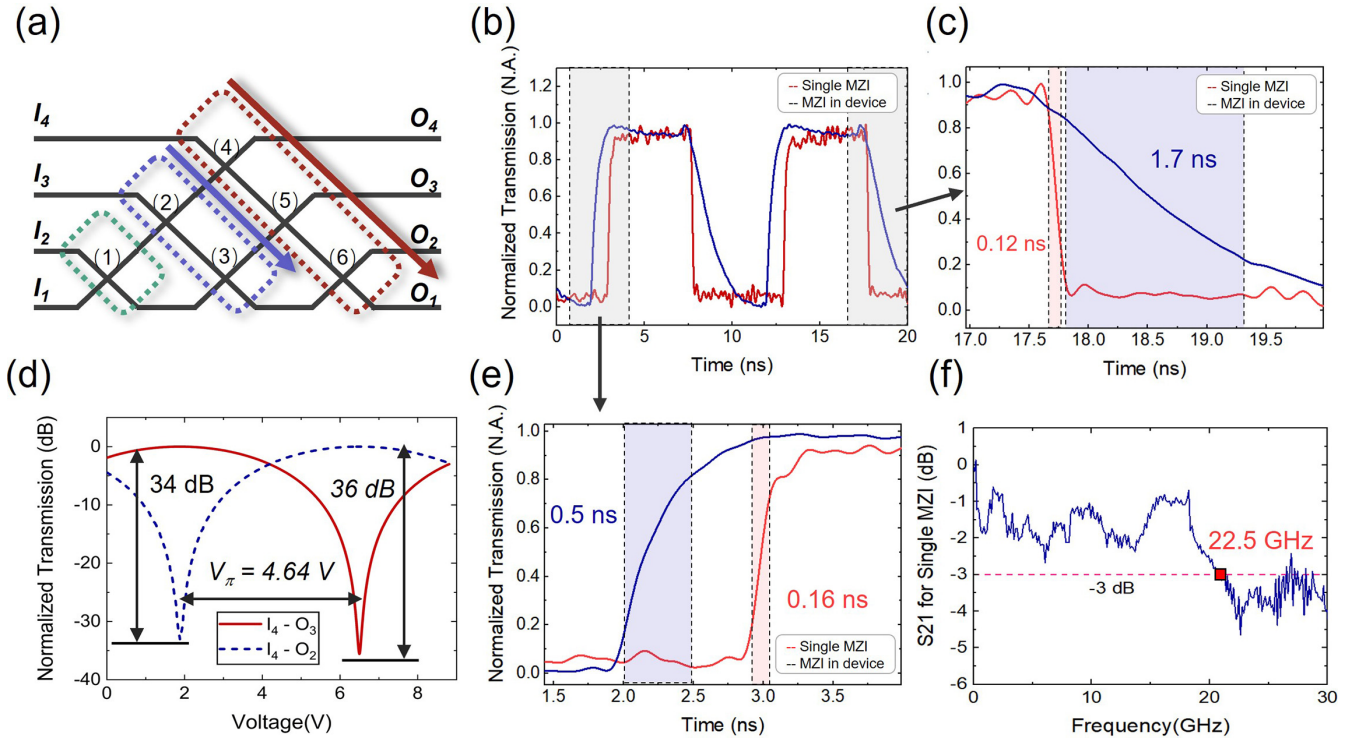

FIG. 3. (a) Schematic of the characterization order of the MZI units in the SU(4). (b) Normalized optical power of the 2 × 2 reconfigurable MZI unit (5) from I_4 input ports to O_3 and O_2 output ports as function of bias voltages. (c) Normalized transmission of route I_4-O_3 with a 100-MHz, 4.4-V peak-to-peak (pk–pk) square wave applied on MZI unit (5) (red line) and a single MZI unit (blue line). (d), (e) Zoom-in view of the rising and the falling edges of the transmission curve, highlighting the rise time of 160 ps and the fall time of 120 ps for the single MZI. (f) Modulation bandwidth of the single MZI unit measured with a VNA. The data shows a 3-dB cutoff at approximately 22.5 GHz.

of 120 ps for the single MZI unit as evidenced in Figs. 3(c) and 3(e), respectively. The electro-optical S21 of the single MZI unit measured using a vector network analyzer (VNA) is shown in Fig. 3(f), indicating a 3-dB bandwidth of 22.5 GHz. The degraded performance of MZI unit (5) in high-frequency response compared to the single MZI unit is mainly caused by the connection circuit between the side pads and the phase shifters of the MZI unit in the multiport interferometer as shown in Fig. 2(a), which are not specifically designed for high-frequency operation and thus suffer large impedance mismatch and microwave loss. It has been well established that with carefully designed traveling wave electrodes, a 3-dB bandwidth above 100 GHz can be readily achieved in LNOI devices [22,24,25], providing enough room to promote the computation power by raising the tuning speed of the MZIs in the future.

The power consumption of EO phase shifters can be analyzed by considering charging and discharging of a capacitor consisting of the GSG electrodes and optical waveguides. The energy dissipated per charge/discharge process can be estimated as $\Delta E_{\mathrm{DISS}} = CV_{DD}^2/2$ [36], in which C is the capacitance of the phase shifters and V_{DD} is the charging voltage. In our device, the capacitance C is calculated as 21 fF, and the V_{DD} is the same as the average half-wave voltage (V_π) of the phase shifters which is measured as 5.38 V, resulting in a power dissipation of 304 fJ for each π-phase shift. Therefore, the power consumption for single phase shifter can be estimated as 60 μW when operating at 100 MHz modulation rate, and the power consumption for the matrix transformation device which contains 24 phase shifters in total can be estimated to be 1.5 mW. It is noteworthy that by carefully designing the GSG electrodes and the waveguides, the power consumption of each phase shifter can be further lowered to ∼0.37 fJ bit^{-1} when operating at 70 Gbit s^{-1} [22].

IV. DEMONSTRATION OF THE LINEAR MATRIX TRANSFORMATION AND DISCUSSION

The programming process of a linear optical processor based on the 4 × 4 reconfigurable MZI as an arbitrary SU(4) is performed by decomposing the linear transformation matrix $[T_{\mathrm{SU}(4)}]$ into the unitary matrices of the corresponding MZI units in the device. The decomposition process is accomplished by successively multiplying $[T_{\mathrm{SU}(4)}]$ with $[D^{(i)}_{\mathrm{MZI}}]^{-1}_{H_{4\times4}}$ in a specific order beginning from the right-hand side, in which $[D^{(i)}_{\mathrm{MZI}}]^{-1}_{H_{4\times4}}$ is the inverse of the unitary transformation matrix of a specific MZI unit. As illustrated in Fig. 4(a), the decomposition process starts from MZI units (1), (2), and (4) [see the red box in Fig. 4(a)] to null all off-diagonal elements in the fourth row and the fourth column of the decomposed matrix by which the effective dimension can be reduced by 1. After that, multiplication of the transmission matrix of MZI units (3) and (5) [the blue box in Fig. 4(a)] and finally (6) [the green box in Fig. 4(a)] will null all the off-diagonal elements, which results in an identity matrix. During the decomposition process, all phase shifts and the corresponding bias voltages for each MZI units in the device can be determined. By measuring the optical power at each output port when

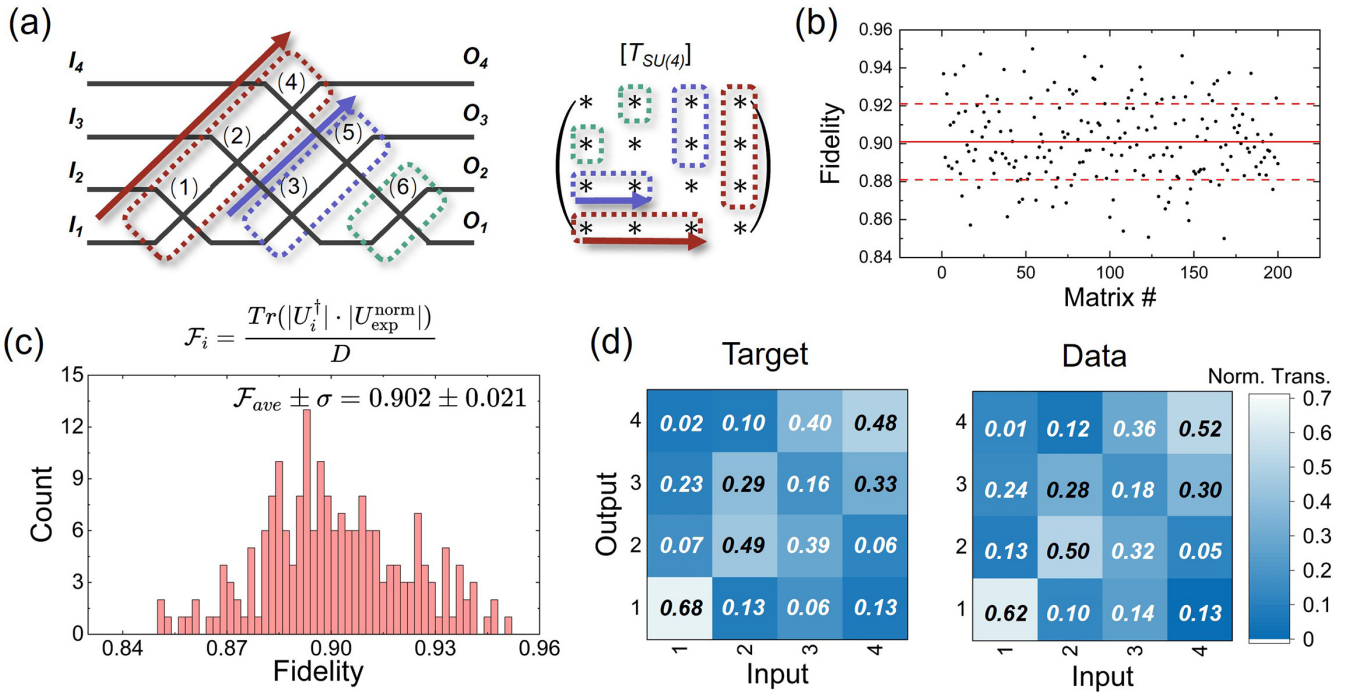

FIG. 4. (a) Schematic illustration of the MZI units order in the SU(4) section for decomposing the unitary transformation matrix $[T_{\text{SU}(4)}]$. (b), (c) Distribution and histogram of the measured fidelity of 200 random matrices. (d) Comparation between one of the ideal target random matrices and the measured results from implementing the target matrix on the fabricated device.

the incident light enters from the input ports (1)–(4) one by one, the normalized optical power from all the different paths can be expressed as a 4×4 transmission matrix $|U_{\text{exp}}|^2$. The performance of the device can be examined by calculating the amplitude fidelity $\mathcal{F}_i = \text{Tr}(|U_i^\dagger||U_{\text{exp}}|)/4$, where U_i is the target matrix [37]. To address the bias drift problem of LN, instead of using a constant bias voltage, we loaded all the bias voltages into 100-MHz synchronous square wave signals, and only a half cycle was recorded from the outports of our device. This approach sacrifices 50% of the modulation rate, avoiding thermal electrodes and maintaining low power consumption.

To confirm the universality of our device, we performed 200 random 4×4 unitary matrixes sampled from the Haar measure into the fabricated chip. The distribution and histogram in Figs. 4(b) and 4(c) show a matrix fidelity of 0.902 $\pm$ 0.021. As an example, Fig. 4(d) compares one of the ideal target random matrices and the measured results from implementing that matrix on our device. The highest contribution to the experimental deviations comes from the fluctuation induced by the vibration of the lensed fibers during the calibration and testing process, which can be further optimized with mode converters integrated on the input and output ends of the programmable photonic circuit.

Table I presents a comparison of the performance of our device to those of the existing state-of-the-art devices based on SOI, silicon nitride, and LNOI platforms. It can be clearly seen that our programmable integrated circuit outperforms the existing devices built upon the SOI and silicon nitride platforms in terms of optical loss, extinction ratio, power consumption, and reconfiguration time. In addition, it is noteworthy that our device is able to achieve extinction ratios exceeding 34 dB using Miller's calibration algorithm, even with the relatively large fabrication fluctuations given by the large footprint of the device. The high tolerance of fabrication imperfections is particularly advantageous for practical applications associated with the VLSPI, where high-precision fabrication may not always be feasible. Last but not least, the scalability of our approach appears optimistic as the performance of the device can be reliably promoted by increasing the number of MZIs to construct larger optical network on the chip and incorporating travelling-wave electrodes to achieve multihundred GHz operation bandwidth. Both approaches will take the device to an unprecedented performance level for both classical and quantum optical computation.

V. CONCLUSION

To conclude, we have demonstrated the fabrication and characterization of a 4×4 programmable linear photonic circuit on the LNOI platform using the PLACE technology. The total on-chip power dissipation is only 1.5 mW when operated at 100-MHz modulation. The MZI units exhibit high performance with large bandwidth of 22.5 GHz, fast switching of a rise time of 160 ps, and a fall time of 120 ps, low insertion loss of 0.15 dB, and high on-chip extinction ratio below -34 dB for both cross and bar routes. Our results demonstrate that LNOI programmable integrated circuits demonstrate superior performance compared to SOI and silicon nitride devices in terms of optical loss, extinction ratio, power consumption, and reconfiguration time. This work provides a significant step towards the realization of large-scale, low-power-consumption, and high-performance photonic circuits for cutting-edge classical and quantum applications.

TABLE I. Comparison of key performance metrics for programmable integrated circuits on different material platforms.

	SOI			SiN				LNOI	
	[2]	[10]	[11]	[12]	[38]	[37]	[39]	This work	[26]
Modes number	26	8	4	4	8	12	20	4	4
Phase shifter Number	176	56	20	12	128	132	380	24	10
Footprint	$4.9 \times 2.4\,\text{mm}^2$			$1.3 \times 0.6\,\text{mm}^2$			$22 \times 30\,\text{mm}^2$	$32 \times 4\,\text{mm}^2$	
MZI loss	0.1 dB	0.4 dB	1.5 dB	3.5 dB	0.2 dB/cm	0.1 dB/cm	0.07 dB/cm	0.15 dB/MZI 0.025 dB/cm	0.8 dB
Extinction ratio	−60 dB	−27 dB	−43 dB @ B.S. −15 dB @ C.S.	−30 dB				−34 dB @ C.S −36 dB @ B.S.	−21 dB
π-Shift power consumption	55 mW	6.1mW	21 mW	200 μW @ 1MHz		385 mW		60 μW @ 100MHz	
Switch time	10 μs	50 μs	30 μs	5 ns		few ms		160 ps Rise 120 ps Fall	
Bandwidth	130 kHz	10 kHz		120 MHz			few kHz	22.6 GHz	6.5 GHz
Average fidelity	0.998				0.919	0.904	0.974	0.902	

Data underlying the results presented in this paper are not publicly available at this time but may be obtained from the authors upon reasonable request.

The authors declare no conflicts of interest.

ACKNOWLEDGMENTS

The authors acknowledge funding from National Key R&D Program of China (Grant No. 2019YFA0705000), National Natural Science Foundation of China (Grants No. 12004116, No. 12104159, No. 11874154, No. 11734009, No. 11933005, No. 12134001, No. 61991444, No. 12204176, and No. 12304418), Science and Technology Commission of Shanghai Municipality (Grant No. 21DZ1101500), Shanghai Municipal Science and Technology Major Project (Grant No. 2019SHZDZX01), Shanghai Sailing Program (Grant No. 21YF1410400), Shanghai Pujiang Program (Grant No. 21PJ1403300), and Innovation Program for Quantum Science and Technology (Grant No. 2021ZD0301403).

APPENDIX

1. Forming an arbitrary SU(N) with cascaded MZIs

The unitary transformation matrix of the MZI units associated with the input and output signals through the respect waveguide channel m and n within the SU(N) can be expressed as

$$[D_{\text{MZI}}(m,n)]_{H_{N\times N}} = \begin{pmatrix} 1 & 0 & \cdots & \cdots & \cdots & \cdots & 0 \\ 0 & 1 & \cdots & \cdots & \cdots & \cdots & 0 \\ \vdots & \vdots & \ddots & \cdots & \vdots & \vdots & \vdots \\ 0 & 0 & \cdots & je^{j(\theta/2)}e^{j\phi}\sin\left(\frac{\theta}{2}\right) & je^{j(\theta/2)}e^{j\phi}\cos\left(\frac{\theta}{2}\right) & \cdots & 0 \\ 0 & 0 & \cdots & \cos\left(\frac{\theta}{2}\right) & -\sin\left(\frac{\theta}{2}\right) & \cdots & 0 \\ \vdots & \vdots & \cdots & \cdots & \cdots & \ddots & \vdots \\ 0 & 0 & \cdots & 0 & 0 & \cdots & 1 \end{pmatrix} \begin{matrix} 1 \\ 2 \\ \vdots \\ m \\ \\ n \\ \vdots \\ N \end{matrix}. \tag{A1}$$

The unitary transformation matrix $[D]_{4\times4}$ can be obtained by the product of the unitary transformation matrices $[D]_{\text{MZI}}$ of MZIs (1)–(6) of which the mathematic form is determined by the order of MZIs in the photonic circuit. Therefore, the unitary transformation matrix $[D]_{4\times4}$ is defined as follows:

$$[D]_{4\times4} = \left[D^{(6)}_{\text{MZI}}\right]_{H_{4\times4}}\left[D^{(5)}_{\text{MZI}}\right]_{H_{4\times4}}\left[D^{(4)}_{\text{MZI}}\right]_{H_{4\times4}}\left[D^{(3)}_{\text{MZI}}\right]_{H_{4\times4}} \times \left[D^{(2)}_{\text{MZI}}\right]_{H_{4\times4}}\left[D^{(1)}_{\text{MZI}}\right]_{H_{4\times4}}. \tag{A2}$$

2. Details of the experimental setup

A polarization controller (Polarization Synthesizer, PSY-201, General Photonics Corp., Chino, California, USA) was used to rotate the light field direction at a wavelength of 1550 nm provided by a continuous laser (CTL 1550, TOPTICA Photonics Inc., Farmington, New York, USA) to transverse-electric (TE) polarization, since the device is designed to operate only with TE-polarized light for the best

TABLE II. Required bias voltages for the cross state and bar state configurations of MZI units in the 4 × 4 programmable linear photonic circuit.

MZI unit		(1)	(2)	(3)	(4)	(5)	(6)
θ	$V_{\text{B.S.}}$ (V)	−8.08	−1.03	−3.97	−2.51	1.87	−5.68
	$V_{\text{C.S.}}$ (V)	−2.38	4.00	2.81	3.12	6.51	−1.09
φ	$V_{\text{B.S.}}$ (V)	−2.46	−0.52	−5.66	4.03	−1.28	
	$V_{\text{C.S.}}$ (V)	4.78	4.46	−0.52	8.99	3.21	

EO-modulation efficiency. Light is coupled in and out of the fabricated device via lensed tapers, and is finally converted to electronic signals using photon detector (APD-2M-A-100K, Luster, Beijing, China), which can be displayed and analyzed on a high-speed real-time oscilloscope (MSO64B, Tektronix Inc., Beaverton, Oregon, USA). The device is electronically programmed using a 64-channel biasing system controlled by an analog output module (PXIe-6739, National Instruments Corp., Austin, Texas, USA).

3. Details of the calibration process

The whole process for calibrating the internal phase shifters begins with MZI units (4)–(6) (red box), and then MZI units (2) and (3) (blue box) before MZI unit (1) (green box), as shown in Fig. 3(a). As an example, we first calibrate MZI unit (4) by applying bias voltages to its internal phase shifter θ_4, as well as the corresponding extra phase shifters θ_{4L} and θ_{4R}. Optical transmission powers through the paths I_4-O_4 and I_4-O_3 were recorded versus the bias voltage applied on the internal phase shifter. The extinction ratios of the paths I_4-O_4 (bar route) and I_4-O_3 (cross route) can be both optimized by repeatedly adjusting the voltages applied on the extra phase shifters θ_{4L} and θ_{4R}, and we can define the bar-state voltage $V_{\text{B.S.}}$ by the applied voltage at which the transmission through the bar path is maximum. Likewise, and the cross-state voltage $V_{\text{C.S.}}$ can be defined by the applied voltage at which the transmission through the cross path is maximum. Afterwards, the bias voltage required for an internal phase shifter to produce a desired phase shift θ can be calculated as

$$V(\theta) = V_{\text{C.S.}} + \frac{\theta |V_{\text{B.S.}} - V_{\text{C.S.}}|}{\pi}. \tag{A3}$$

To calibrate the outer phase shifters, the corresponding MZI unit and the subsequent MZI unit will be set as 50:50 beam splitters to form another MZI, and the MZI units on each arm of the newly formed MZI will operate in the bar state. For example, during the calibration process of the phase shifter φ_2, MZI units (2) and (5) will be set as 50:50 beam splitters and MZI units (4) and (3) will operate in the bar state. Phase shifter φ_4 can also be calibrated using the same protocol considering the configuration of the push-pull electrodes. Using the same process, φ_3 and φ_5 can be calibrated in the MZI formed with MZI units (3) and (6) by operating MZI unit (5) in the bar state. Despite the fact that φ_6 cannot be calibrated in our device, this does not affect the final test results, since it only introduces an unknown constant phase to the output light.

The details of the calibration process can be found in Methods section as well. Table II presents the required bias voltages for the cross state and bar state configurations of the MZI-units in the 4 × 4 programmable linear photonic circuit.

4. Details of the decomposition process

It is essential to point out that we can always find a $[D^{(i)}_{\text{MZI}}]^{-1}_{H_{4\times4}}$ such that in each step of the successive multiplications of $[T_{\text{SU(4)}}]$ with $[D^{(i)}_{\text{MZI}}]^{-1}_{H_{4\times4}}$, an off-diagonal element in the lower triangle of the resultant matrix becomes zero, i.e., the multiplication of an arbitrary $[T_{\text{SU(4)}}]$ with $[D^{(1)}_{\text{MZI}}]^{-1}_{H_{4\times4}}$ can be expressed as follows:

$$[T_{\text{SU(4)}}]\left[D^{(1)}_{\text{MZI}}\right]^{-1}_{H_{4\times4}} = \begin{pmatrix} U_{11} & U_{12} & U_{13} & U_{14} \\ U_{21} & U_{22} & U_{23} & U_{24} \\ U_{31} & U_{32} & U_{33} & U_{34} \\ U_{41} & U_{42} & U_{43} & U_{44} \end{pmatrix} - je^{-j(\theta_1/2)} \begin{pmatrix} e^{-j\varphi_1}\sin\left(\frac{\theta_1}{2}\right) & \cos\left(\frac{\theta_1}{2}\right) & 0 & 0 \\ e^{-j\varphi_1}\cos\left(\frac{\theta_1}{2}\right) & -\sin\left(\frac{\theta_1}{2}\right) & 0 & 0 \\ 0 & 0 & 1 & 0 \\ 0 & 0 & 0 & 1 \end{pmatrix} = \begin{pmatrix} * & * & * & * \\ * & * & * & * \\ * & * & * & * \\ 0 & * & * & * \end{pmatrix},$$

$$\text{if}: \ \theta_1 = 2\arctan\left(\frac{-U_{42}}{U_{41}}\right). \tag{A4}$$

As illustrated in Fig. 4(a), the decomposition process starts from MZIs (1), (2), and (4) [red box in Fig. 4(a)], which will null the first, second, and third element in the fourth row of the decomposed matrix, respectively. Because of the unitary property of the decomposed matrix, when all off-diagonal elements become zero, the off-diagonal elements in the corresponding column also become zero in each row. Thus, the effective dimension of the decomposed matrix can be reduced

by 1 as follows:

$$[T_{SU(4)}]\left[D^{(1)}_{\mathrm{MZI}}\right]^{-1}_{H_{4\times4}}\left[D^{(2)}_{\mathrm{MZI}}\right]^{-1}_{H_{4\times4}}\left[D^{(4)}_{\mathrm{MZI}}\right]^{-1}_{H_{4\times4}} = \begin{pmatrix} & & & 0 \\ (& T_{\mathrm{SU(3)}} &) & 0 \\ & & & 0 \\ 0 & 0 & 0 & 1 \end{pmatrix}. \quad \text{(A5)}$$

The next step is to multiply the transmission matrix of MZIs (3) and then (5) to reduce the effective dimension of the resultant matrix to two dimensions [blue box in Fig. 4(a)]. Finally, the multiplication of the decomposed matrix by $[D^{(6)}_{\mathrm{MZI}}]^{-1}_{H_{4\times4}}$ will null all the off-diagonal elements, resulting in an identity matrix [green box in Fig. 4(a)]. Thus,

$$[T_{\mathrm{SU(4)}}]\left[D^{(1)}_{\mathrm{MZI}}\right]^{-1}_{H_{4\times4}}\left[D^{(2)}_{\mathrm{MZI}}\right]^{-1}_{H_{4\times4}}\left[D^{(4)}_{\mathrm{MZI}}\right]^{-1}_{H_{4\times4}} \times\left[D^{(3)}_{\mathrm{MZI}}\right]^{-1}_{H_{4\times4}}\left[D^{(5)}_{\mathrm{MZI}}\right]^{-1}_{H_{4\times4}}\left[D^{(6)}_{\mathrm{MZI}}\right]^{-1}_{H_{4\times4}} = [I]_{4\times4}. \quad \text{(A6)}$$

TABLE III. Calculated phase shifts and the corresponding bias voltages of the MZIs for programming the SU(4)s.

MZI	(1)	(2)	(3)	(4)	(5)	(6)
θ (Rad)	−2.68	2.08	−0.34	1.76	−1.85	−0.65
V_θ (*V*)	4.16	7.32	2.08	6.27	3.78	7.15
φ (Rad)	0.92	−0.21	−0.79	0.17	0.61	−0.53
V_φ (*V*)	6.91	4.13	8.46	9.26	4.09	

Equation (5) is equivalent to Eq. (1), therefore, all the required phase shifts to implement any arbitrary SU(4) are obtained after the decomposition process. The required phase shifts for the phase shifters of the MZI units in the device to implement the two SU(4)s in the main text were obtained by the decomposition process mentioned above. Table III lists the required phase shifts and the corresponding bias voltages for each MZI units.

[1] Y. Shen, N. C. Harris, S. Skirlo, M. Prabhu, T. Baehr-Jones, M. Hochberg, X. Sun, S. Zhao, H. Larochelle, D. Englund, and M. Soljačić, Deep learning with coherent nanophotonic circuits, Nat. Photonics **11**, 441 (2017).

[2] N. C. Harris, G. R. Steinbrecher, M. Prabhu, Y. Lahini, J. Mower, D. Bunandar, C. Chen, F. N. C. Wong, T. Baehr-Jones, M. Hochberg, S. Lloyd, and D. Englund, Quantum transport simulations in a programmable nanophotonic processor, Nat. Photonics **11**, 447 (2017).

[3] D. Pérez, I. Gasulla, L. Crudgington, D. J. Thomson, A. Z. Khokhar, K. Li, W. Cao, G. Z. Mashanovich, and J. Capmany, Multipurpose silicon photonics signal processor core, Nat. Commun. **8**, 636 (2017).

[4] G. Wetzstein, A. Ozcan, S. Gigan, S. Fan, D. Englund, M. Soljačić, C. Denz, D. A. B. Miller, and D. Psaltis, Inference in artificial intelligence with deep optics and photonics, Nature (London) **588**, 39 (2020).

[5] B. J. Shastri, A. N. Tait, T. Ferreira de Lima, W. H. P. Pernice, H. Bhaskaran, C. D. Wright, and P. R. Prucnal, Photonics for artificial intelligence and neuromorphic computing, Nat. Photonics **15**, 102 (2021).

[6] X. Xu, L. Zhu, W. Zhuang, D. Zhang, P. Yuan, and L. Lu, Photoelectric hybrid convolution neural network with coherent nanophotonic circuits, Opt. Eng. **60**, 117106 (2021).

[7] R. Shao, G. Zhang, and X. Gong, Generalized robust training scheme using genetic algorithm for optical neural networks with imprecise components, Photon. Res. **10**, 1868 (2022).

[8] N. C. Harris, J. Carolan, D. Bunandar, M. Prabhu, M. Hochberg, T. Baehr-Jones, M. L. Fanto, A. M. Smith, C. C. Tison, P. M. Alsing, and D. Englund, Linear programmable nanophotonic processors, Optica **5**, 1623 (2018).

[9] H. Zhou, Y. Zhao, G. Xu, X. Wang, Z. Tan, J. Dong, and X. Zhang, Chip-scale optical matrix computation for pagerank algorithm, IEEE J. Sel. Top. Quantum Electron. **26**, 8300910 (2020).

[10] H. Zhang, M. Gu, X. D. Jiang, J. Thompson, H. Cai, S. Paesani, R. Santagati, A. Laing, Y. Zhang, M. H. Yung, Y. Z. Shi, F. K. Muhammad, G. Q. Lo, X. S. Luo, B. Dong, D. L. Kwong, L. C. Kwek, and A. Q. Liu, An optical neural chip for implementing complex-valued neural network, Nat. Commun. **12**, 457 (2021).

[11] F. Shokraneh, M. S. Nezami, and O. Liboiron-Ladouceur, Theoretical and experimental analysis of a 4×4 reconfigurable mzi-based linear optical processor, J. Lightwave Technol. **38**, 1258 (2020).

[12] M. Dong, G. Clark, A. J. Leenheer, M. Zimmermann, D. Dominguez, A. J. Menssen, D. Heim, G. Gilbert, D. Englund, and M. Eichenfield, High-speed programmable photonic circuits in a cryogenically compatible, visible–near-infrared 200 mm CMOS architecture, Nat. Photonics **16**, 59 (2022).

[13] W. Ma, Z. Liu, Z. A. Kudyshev, A. Boltasseva, W. Cai, and Y. Liu, Deep learning for the design of photonic structures, Nat. Photonics **15**, 77 (2021).

[14] D. A. B. Miller, Analyzing and generating multimode optical fields using self-configuring networks, Optica **7**, 794 (2020).

[15] S. Pai, Z. Sun, T. W. Hughes, T. Park, B. Bartlett, I. A. D. Williamson, M. Minkov, M. Milanizadeh, N. Abebe, F. Morichetti, A. Melloni, S. Fan, O. Solgaard, and D. A. B. Miller, Experimentally realized in situ backpropagation for deep learning in photonic neural networks, Science **380**, 398 (2023).

[16] S. Pai, O. Solgaard, S. Fan, and D. Miller, Scalable and self-correcting photonic computation using balanced photonic binary tree cascades, arXiv:2210.16935.

[17] S. Bandyopadhyay, A. Sludds, S. Krastanov, R. Hamerly, N. Harris, D. Bunandar, M. Streshinsky, M. Hochberg, and D. Englund, Single chip photonic deep neural network with accelerated training, arXiv:2208.01623.

[18] R. Hamerly, S. Bandyopadhyay, and D. Englund, Stability of Self-Configuring Large Multiport Interferometers, Phys. Rev. Appl. **18**, 024018 (2022).

[19] M. Reck, A. Zeilinger, H. J. Bernstein, and P. Bertani, Experimental Realization of Any Discrete Unitary Operator, Phys. Rev. Lett. **73**, 58 (1994).

[20] D. Zhu, L. Shao, M. Yu, R. Cheng, B. Desiatov, C. J. Xin, Y. Hu, J. Holzgrafe, S. Ghosh, A. Shams-Ansari, E. Puma, N. Sinclair, C. Reimer, M. Zhang, and M. Lončar, Integrated photonics on thin-film lithium niobate, Adv. Opt. Photon. **13**, 242 (2021).

[21] Y. Jia, L. Wang, and F. Chen, Ion-cut lithium niobate on insulator technology: Recent advances and perspectives, Appl. Phys. Rev. **8**, 011307 (2021).

[22] C. Wang, M. Zhang, X. Chen, M. Bertrand, A. Shams-Ansari, S. Chandrasekhar, P. Winzer, and M. Lončar, Integrated lithium niobate electro-optic modulators operating at CMOS-compatible voltages, Nature (London) **562**, 101 (2018).

[23] M. Xu, M. He, H. Zhang, J. Jian, Y. Pan, X. Liu, L. Chen, X. Meng, H. Chen, Z. Li, X. Xiao, S. Yu, S. Yu, and X. Cai, High-performance coherent optical modulators based on thin-film lithium niobate platform, Nat. Commun. **11**, 3911 (2020).

[24] M. He, M. Xu, Y. Ren, J. Jian, Z. Ruan, Y. Xu, S. Gao, S. Sun, X. Wen, L. Zhou, L. Liu, C. Guo, H. Chen, S. Yu, L. Liu, and X. Cai, High-performance hybrid silicon and lithium niobate Mach–Zehnder modulators for 100 Gbit s^{-1} and beyond, Nat. Photonics **13**, 359 (2019).

[25] P. Kharel, C. Reimer, K. Luke, L. He, and M. Zhang, Breaking voltage–bandwidth limits in integrated lithium niobate modulators using micro-structured electrodes, Optica **8**, 357 (2021).

[26] P. I. Sund, E. Lomonte, S. Paesani, Y. Wang, J. Carolan, N. Bart, A. D. Wieck, A. Ludwig, L. Midolo, W. H. P. Pernice, P. Lodahl, and F. Lenzini, High-speed thin-film lithium niobate quantum processor driven by a solid-state quantum emitter, Sci. Adv. **9**, eadg7268 (2023).

[27] J. Zhou, R. Gao, J. Lin, M. Wang, W. Chu, W. Li, D. Yin, L. Deng, Z. Fang, and J. Zhang, Electro-optically switchable optical true delay lines of meter-scale lengths fabricated on lithium niobate on insulator using photolithography assisted chemo-mechanical etching, Chin. Phys. Lett. **37**, 084201 (2020).

[28] L. Song, J. Chen, R. Wu, Y. Zheng, Z. Liu, G. Wang, C. Sun, M. Wang, and Y. Cheng, Electro-optically tunable optical delay line with a continuous tuning range of ∼220 fs in thin-film lithium niobate, Opt. Lett. **48**, 2261 (2023).

[29] J. Lu, M. Li, C.-L. Zou, A. A. Sayem, and H. X. Tang, Toward 1% single-photon anharmonicity with periodically poled lithium niobate microring resonators, arXiv:2203.01801.

[30] M. Zhang, B. Buscaino, C. Wang, A. Shams-Ansari, C. Reimer, R. Zhu, J. M. Kahn, and M. Lončar, Broadband electro-optic frequency comb generation in a lithium niobate microring resonator, Nature (London) **568**, 373 (2019).

[31] Y. Zhou, Z. Wang, Z. Fang, Z. Liu, H. Zhang, D. Yin, Y. Liang, Z. Zhang, J. Liu, and T. Huang, On-chip microdisk laser on Yb 3+-doped thin-film lithium niobate, Opt. Lett. **46**, 5651 (2021).

[32] Y. Liang, J. Zhou, Z. Liu, H. Zhang, Z. Fang, Y. Zhou, D. Yin, J. Lin, J. Yu, and R. Wu, and others, A high-gain cladded waveguide amplifier on erbium doped thin-film lithium niobate fabricated using photolithography assisted chemo-mechanical etching, Nanophotonics **11**, 1033 (2022).

[33] K. Luke, P. Kharel, C. Reimer, L. He, M. Loncar, and M. Zhang, Wafer-scale low-loss lithium niobate photonic integrated circuits, Opt. Express **28**, 24452 (2020).

[34] M. Wang, R. Wu, J. Lin, J. Zhang, Z. Fang, Z. Chai, and Y. Cheng, Chemo-mechanical polish lithography: A pathway to low loss large-scale photonic integration on lithium niobate on insulator, Quantum Eng. **1**, e9 (2019).

[35] R. Wu, L. Gao, Y. Liang, Y. Zheng, J. Zhou, H. Qi, D. Yin, M. Wang, Z. Fang, and Y. Cheng, High-Production-Rate fabrication of low-loss lithium niobate electro-optic modulators using photolithography assisted chemo-mechanical etching (PLACE), Micromachines **13**, 378 (2022).

[36] D. A. B. Miller, Energy consumption in optical modulators for interconnects, Opt. Express **20**, A293 (2012).

[37] C. Taballione, R. van der Meer, H. J. Snijders, P. Hooijschuur, J. P. Epping, M. de Goede, B. Kassenberg, P. Venderbosch, C. Toebes, H. van den Vlekkert, P. W. H. Pinkse, and J. J. Renema, A universal fully reconfigurable 12-mode quantum photonic processor, Mater. Quantum. Technol. **1**, 035002 (2021).

[38] C. Taballione, T. A. W. Wolterink, J. Lugani, A. Eckstein, B. A. Bell, R. Grootjans, I. Visscher, D. Geskus, C. G. H. Roeloffzen, J. J. Renema, I. A. Walmsley, P. W. H. Pinkse, and K.-J. Boller, 8 × 8 reconfigurable quantum photonic processor based on silicon nitride waveguides, Opt. Express **27**, 26842 (2019).

[39] C. Taballione, M. C. Anguita, M. de Goede, P. Venderbosch, B. Kassenberg, H. Snijders, N. Kannan, W. L. Vleeshouwers, D. Smith, J. P. Epping, R. van der Meer, P. W. H. Pinkse, H. van den Vlekkert, and J. J. Renema, 20-Mode universal quantum photonic processor, arXiv:2203.01801 [quant-ph] (2023).

Correction: The title contained a typographical error and has been fixed.